Chemical Science

Accepted Manuscript

ROYAL SOCIETY OF CHEMISTRY

rsc.li/chemical-science

View Article Online
DOI: 10.1039/D5SC08298F

ARTICLE

Alkaline-adaptive covalent organic framework photocatalysts: synergistic molecular orbital and hydrogen-bond network engineering for H_2O_2 production

Received 00th January 20xx,
Accepted 00th January 20xx

DOI: 10.1039/x0xx00000x

Zhiwu Yu, [a] *Jiayi Zhang,* [a] *Xiaolong Zhang,* [a] *Xuwen Sun,* [a] *Guihong Wu,* [b] *Zhiyun Zhang,* [a] *Fengtao Yu**[b] *and Jianli Hua**[a]

Abstract: Alkaline hydrogen peroxide (H_2O_2) is highly desirable for critical applications due to its superior stability and reactivity, but is incompatible with conventional near-neutral production methods. While covalent organic frameworks (COFs) show promise for photocatalytic H_2O_2 generation, their alkaline performance is severely limited by poor charge dynamics and inadequate hydrophilicity, hindering the essential 2e⁻ oxygen reduction reaction (ORR: $O_2 + 2e^- + H_2O \rightarrow HO_2^- + OH^-$) and 4e⁻ water oxidation reaction (WOR: $4OH^- \rightarrow O_2 + 2H_2O + 4e^-$). This work pioneers a dual-engineering strategy (molecular orbital and interfacial hydrogen-bonding network engineering) within *β*-ketoenamine-linked COFs to overcome these challenges simultaneously. By contrasting phenazine-based (TP-PZ-COF) and anthracene-based (TP-AN-COF) COFs, we demonstrate that strategic integration of sp^2-N heteroatoms modulates molecular orbitals and enhances $n\rightarrow\pi^*$ transitions, optimizing charge separation and transport for efficient 2e⁻ ORR and 4e⁻ WOR. Concurrently, the planar phenazine units form robust hydrogen-bonding networks that dramatically boost hydroxide ion (OH^-) affinity and interfacial enrichment, thereby accelerating 4e⁻ WOR kinetics. This integrated approach enabled TP-PZ-COF to achieve an exceptional alkaline H_2O_2 production rate of 4961 μmol g^{-1} h^{-1} under 0.01 M NaOH, representing an 8.1-fold increase over TP-AN-COF (606 μmolg^{-1} h^{-1}). The generated H_2O_2 efficiently degraded industrial dye pollutants. Direct experimental and theoretical validations confirmed the cooperative mechanism between charge dynamics optimization and OH^- affinity enhancement, providing a new blueprint for designing on-demand alkaline H_2O_2 photocatalysts.

Introduction

Hydrogen peroxide, a green oxidant decomposing solely to water and oxygen, is essential for applications like pulp bleaching[1], disinfection[2], organic synthesis[3], and environmental remediation[4]. Its utilization under alkaline conditions is particularly advantageous, enhancing stability and facilitating the generation of highly reactive hydroxyl radicals (·OH), thereby boosting efficiency in advanced oxidation processes, selective transformations, and electrochemical sensing.[5-7] However, conventional H_2O_2 production relies heavily on the energy-intensive anthraquinone process, which inherently yields near-neutral H_2O_2.[8, 9]This fundamental limitation prevents the immediate exploitation of alkaline H_2O_2 superior reactivity and stability in distributed applications.[10] Consequently, developing efficient photocatalytic systems for direct alkaline H_2O_2 generation is not just beneficial but urgently necessary for sustainable, on-site production in its most effective form.

COFs have rapidly emerged as premier photocatalysts for H_2O_2 production due to their crystalline order, exceptional tunability, photostability, and abundant functional sites.[11-13] Unlike traditional inorganic semiconductors, COFs offer unparalleled molecular-level control over electronic structure and active sites through rational backbone and linker design.[14-17] This enables precise optimization of light harvesting, charge carrier generation, and catalytic activity specifically for H_2O_2 synthesis.[18-21] Nevertheless, deploying COFs under the desirable alkaline conditions presents significant hurdles: (i) inefficient charge separation and transfer kinetics, which severely hinder the critical two-electron oxygen reduction reaction (2e⁻ ORR) pathway; (ii) often insufficient hydrophilicity, which critically limits the adsorption of OH^- and consequently hampers the formation of efficient reactant interfaces, drastically retarding 4e⁻ WOR kinetics; and (iii) inadequate chemical and structural stability in strongly basic environments, where framework degradation or active-site deactivation often leads to rapid performance decay during photocatalysis. These combined limitations fundamentally bottleneck the overall photocatalytic H_2O_2 yield in alkaline media. Building upon the identified challenges in alkaline environments, modulating molecular orbitals and constructing hydrogen-bonding networks within COFs emerge as particularly promising strategies to

[a] *Key Laboratory for Advanced Materials and Joint International Research Laboratory for Precision Chemistry and Molecular Engineering, Feringa Nobel Prize Scientist Joint Research Center, Frontiers Science Center for Materiobiology and Dynamic Chemistry, School of Chemistry and Molecular Engineering, East China University of Science and Technology, Shanghai, 200237, China. E-mail: jlhua@ecust.edu.cn*
[b] *Jiangxi Province Key Laboratory of Functional Organic Polymers, East China University of Technology, Nanchang, 330013, China. E-mail: fty853815622@ecut.edu.cn*

Supplementary Information available: [details of any supplementary information available should be included here]. See DOI: 10.1039/x0xx00000x

View Article Online
DOI: 10.1039/D5SC08229E

overcome these bottlenecks and enhance photocatalytic H_2O_2 production.[22-25] Molecular orbital engineering, achieved through heteroatom incorporation (e.g., N, S, O) into the COF backbone, directly targets electronic structure and energy level optimization.[26, 27] This approach holds significant potential to address inefficient charge separation and transfer which was key factors currently limiting the $2e^-$ ORR pathway, thereby improving light harvesting, promoting exciton dissociation, and facilitating charge carrier transport. Simultaneously, the strategic introduction of robust hydrogen-bonding networks offers a potent solution to the critical issue of insufficient hydrophilicity under alkaline conditions.[28] These networks enhance water/ion affinity, promote the targeted enrichment of reactive OH^-, accelerate intermediate conversion, and reduce energy barriers, effectively mitigating the slow $4e^-$ WOR kinetics caused by poor OH^- adsorption and interfacial inefficiency.[29, 30] While existing phenazine-COFs and β-ketoenamine COFs can address certain individual limitations, they still suffer from single, isolated shortcomings under strongly alkaline conditions, such as limited charge separation, insufficient OH^- adsorption, or low H_2O_2 stability, which restrict their overall photocatalytic performance. While each strategy individually tackles specific bottlenecks, the synergistic integration of molecular orbital engineering and hydrogen-bonding network construction within a single COF system remains largely unexplored but highly promising for efficient alkaline photocatalytic H_2O_2 generation.

Herein, we developed a dual-engineering strategy integrating both approaches within β-ketoenamine-linked COFs. Two structurally analogous COFs TP-AN-COF and TP-PZ-COF, which was different only in two linker atoms, were synthesized for direct performance evaluation (Fig. 1a). The phenazine-based TP-PZ-COF demonstrated substantially enhanced photocatalytic activity, attributed synergistically to: (i) expanded $n \rightarrow \pi^*$ excitation channels optimizing charge dynamics, and (ii) planar sp^2-hybridized nitrogen atoms establishing robust hydrogen bonds with H_2O/OH^- (Fig. 1b). Beyond improving reaction kinetics, these hydrogen-bonding interactions help stabilize the local chemical environment of the framework, thereby enhancing the structural durability of the COF in strongly alkaline media. This dual functionality collectively addressed prior bottlenecks, enhancing charge separation for efficient $2e^-$ ORR while accelerating OH^- enrichment and activation for improved WOR kinetics. Under alkaline conditions (0.01 M NaOH), TP-PZ-COF achieved an exceptional H_2O_2 production rate of 4961 μmol g^{-1} h^{-1}, surpassing TP-AN-COF by 8.1-fold. The practical utility of this alkaline-generated H_2O_2 was further demonstrated through effective degradation of metal-containing dyes (e.g., Rhodamine B, Rose Bengal) in industrial wastewater. Transient absorption spectroscopy (TAS) and density functional theory (DFT) calculations unambiguously revealed the cooperative mechanism: molecular orbital modulation directs charge transfer pathways, while hydrogen-bond networks facilitate reactant interfacial dynamics. This work establishes a new design paradigm for COF photocatalysts targeting efficient on-demand H_2O_2 synthesis in alkaline environments.

Results and Discussion

TP-AN-COF was synthesized by a typical Shiff-base condensation reaction between 1,3,5-triformylphloroglucinol (TFP) and 2,6-anthracenediamine, while TP-PZ-COF was obtained via an imine-exchange reaction between TFP and 2,7-diaminophenazine·benzylideneaniline (DAPH·Bnzph).[31] The chemical structures of both COFs were systematically characterized using Fourier-transform infrared (FT-IR) spectroscopy, solid-state ^{13}C nuclear magnetic resonance (^{13}C NMR), and X-ray photoelectron spectroscopy (XPS). The formation of *β*-ketoenamine linkages in both frameworks was confirmed by FT-IR analysis (Fig. S2†). Specifically, characteristic stretching bands corresponding to C=O appeared at ~1583 cm^{-1}, while C–N stretching vibrations were observed at 1261 and 1269 cm^{-1}. Additionally, a distinct absorption peak at ~1163 cm^{-1} was assigned to the phenazine (PZ) moiety (Fig. 2a).[32] Solid-state ^{13}C NMR spectra further corroborated the formation of *β*-ketoenamine linkages, showing signals at ~183 ppm for C=O, ~105 ppm for C=C–NH, and ~145 ppm for =C–NH carbons (Fig. 2b). High-resolution XPS analysis provided additional evidence for the successful construction of the two COF structures (Fig. 2c and S4 †). For TP-AN-COF, the N 1s spectrum showed a single deconvoluted peak at 400.28 eV, corresponding to sp^3-hybridized N in C–N bonds of the *β*-ketoenamine linkage. In contrast, TP-PZ-COF displayed a new peak at 398.98 eV, attributable to sp^2-hybridized N (C=N), confirming the successful incorporation of the PZ units into the COF. The crystalline structures of TP-PZ-COF and TP-AN-COF were investigated by powder X-ray diffraction (PXRD), as shown in Fig. 2d and 2g. TP-PZ-COF exhibited distinct diffraction peaks at 3.38°, 5.86°, and 23.8°, corresponding to the (100), (110), and (001) crystal planes, respectively. Similarly, TP-AN-COF displayed diffraction peaks at 3.34°, 5.79°, and 23.8°, assignable to the (100), (110), and (001) facets. Both COFs presented comparable crystalline domain sizes, as summarized in Table S1 and S2 †. The experimental PXRD patterns were in excellent agreement with simulated diffraction profiles based on an AA stacking model (Fig. S5 and S6†). The refined unit cell parameters were as follows: TP-PZ-COF, a = b = 30.15 Å, c = 3.74 Å, α = β = 90.00°, γ = 120.00°, with residuals R_{wp} = 6.97% and R_p = 5.33%; TP-AN-COF, a = b = 30.48 Å, c = 3.72 Å, α = β = 90.00°, γ = 120.00°, with residuals R_{wp} = 6.45% and R_p = 4.87%. These results clearly confirm that both COFs possess highly ordered crystalline structures with well-defined, predesigned topologies.[33]

The porous structures of TP-PZ-COF and TP-AN-COF were investigated by N_2 adsorption–desorption measurements. As shown in Fig. 2e and 2h †, both COFs exhibit typical type-I isotherms, indicative of microporous structures. The Brunauer–Emmett–Teller (BET) surface areas were determined to be 1032 m^2 g^{-1} for TP-PZ-COF and 940 m^2 g^{-1} for TP-AN-COF, providing a comparable basis for evaluating their photocatalytic performance. Pore size distribution analyses based on nonlocal density functional theory (NLDFT) with a cylindrical pore model revealed distinct peaks centered at 1.27 and 1.35 nm for TP-PZ-COF and TP-AN-COF. Such microporous architectures are favorable for constructing hydrogen-bonded networks and facilitating the diffusion of O_2 and OH^- ions, thereby enhancing photocatalytic H_2O_2 generation under alkaline conditions.[34] Scanning electron microscopy (SEM) images revealed that TP-PZ-COF adopted a partially flexible rod-like morphology (Fig. 2f and S7†), while TP-AN-COF exhibited a sheet-like morphology (Fig. 2i and S8†), suggesting that the PZ unit confers greater structural

View Article Online
DOI: 10.1039/D5SC08298F

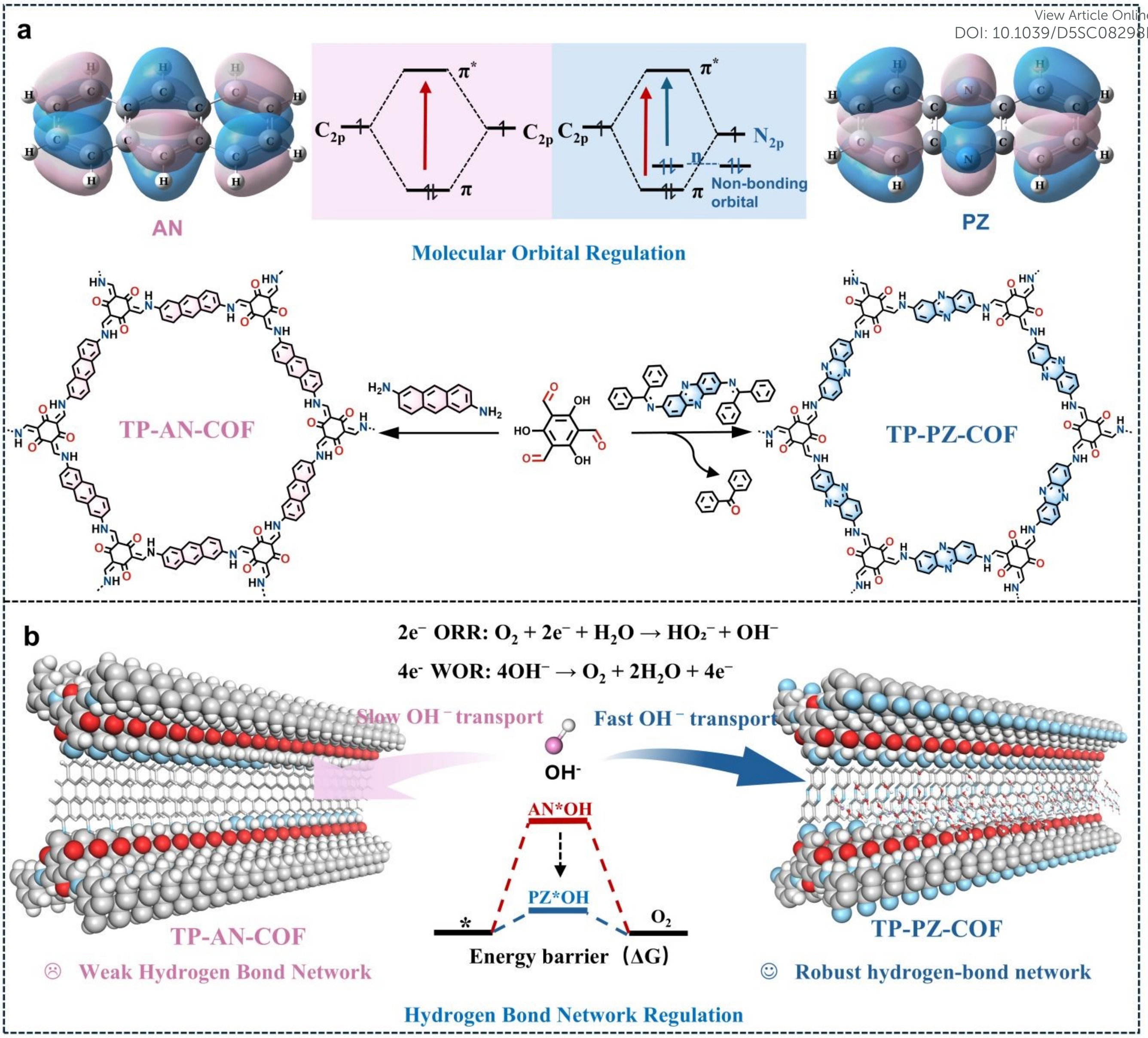

Fig. 1 (a) Synthetic routes and corresponding chemical structures of TP-PZ-COF and TP-AN-COF. (b)Transitions and arrangement of molecular orbitals in AN and PZ. (c) Engineering of Hydrogen-Bonding Networks.

flexibility than the anthracene (AN) counterpart. High-resolution transmission electron microscopy (HR-TEM) confirmed the high crystallinity of both COFs, with well-resolved lattice fringes corresponding to interplanar spacings of 2.16 and 2.10 nm for TP-PZ-COF and TP-AN-COF (insets in Fig. 2f and 2i†).[35]

The band structure of a photocatalyst, especially the positions of the valence band (VB) and conduction band (CB), critically influences its photocatalytic performance by determining the thermodynamic driving force of the reaction.[36, 37] Since the band-edge positions are pH-dependent, it is essential to characterize both COF materials under their actual operating pH conditions to accurately evaluate their electronic structures.[38] As shown in Fig. 3a, TP-PZ-COF exhibited a broader UV–vis absorption profile compared to the conventional anthracene-based TP-AN-COF, which could be attributed to the strong electron-withdrawing effect of the nitrogen-containing aromatic heterocycles. Based on the absorption edges, the optical bandgaps of TP-PZ-COF and TP-AN-COF were estimated to be 1.74 and 2.03 eV, respectively (inset in Fig. 3a). The Mott–Schottky plots of both COFs show positive slopes, confirming their n-type semiconducting nature (Fig. S9†). Under alkaline conditions (pH = 12) using Ag/AgCl as the reference electrode, the flat-band potentials (E_{fb}) of TP-PZ-COF and TP-AN-COF were determined to be −0.62 eV and −0.65 eV, respectively. For n-type semiconductors, the CB edge is typically located approximately 0.20 V more negative than the flat-band potential. Accordingly, the CB positions of TP-PZ-COF and TP-AN-COF were estimated to be −0.42 eV and −0.45 eV (vs NHE, pH = 12), respectively. Combining these values with the optical bandgaps, the VB positions were calculated using $E_{VB} = E_{CB} + E_g$,

View Article Online
DOI: 10.1039/D5SC08798F

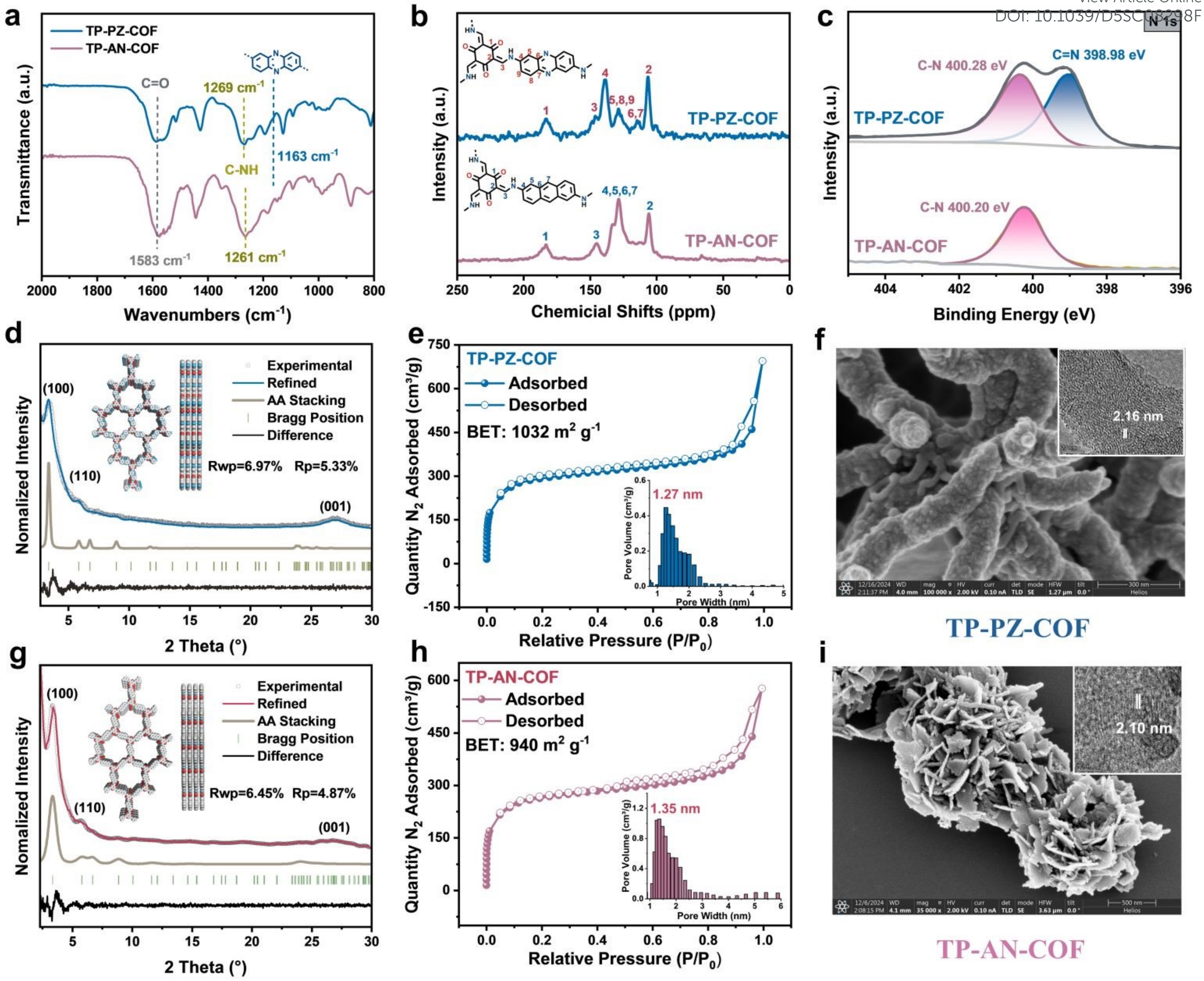

Fig. 2 (a) FT-IR spectrum of TP-PZ-COF and TP-AN-COF. (b) Solid-state ^{13}C CP/MAS-NMR spectra of TP-PZ-COF and TP-AN-COF. (c) The XPS spectra of N 1s for TP-PZ-COF and TP-AN-COF. (d) PXRD patterns of TP-PZ-COF. (e) N_2 adsorption-desorption isotherms at 77.3 K and Pore size distribution(inset) for TP-PZ-COF. (f) SEM and HR-TEM image(inset) of TP-PZ-COF. (g) PXRD patterns of TP-AN-COF. (h) N_2 adsorption-desorption isotherms at 77.3 K and Pore size distribution(inset) for TP-AN-COF. (i) SEM and HR-TEM image(inset) of TP-PZ-COF.

yielding 1.32 and 1.58 eV for TP-PZ-COF and TP-AN-COF (vs NHE, pH = 12). Considering the standard redox potentials under alkaline conditions (pH = 12), including $O_2/\cdot O_2^-$ (−0.33 eV), O_2/HO_2^- (+0.519 eV), and OH^-/O_2 (−0.522 eV), the band structures of both COFs are thermodynamically favorable for overall photocatalytic H_2O_2 production (Fig. 3b).[39, 40] Both materials can facilitate H_2O_2 generation through 2e⁻ ORR ($O_2 + 2e^- + H_2O \rightarrow HO_2^- + OH^-$) coupled with the 4e⁻ WOR ($4OH^- \rightarrow O_2 + 2H_2O + 4e^-$).[41] The photocatalytic H_2O_2 production performance of TP-PZ-COF and TP-AN-COF was evaluated under visible-light irradiation (λ > 420 nm, 300 W Xe lamp) without any sacrificial agent, in air and NaOH solutions of different pH values (Fig. S1 and S10†). The results showed that both COFs exhibited the highest activity at pH = 12. Notably, under O_2-saturated alkaline conditions (pH = 12), TP-PZ-COF achieved a H_2O_2 production rate of 4961 μmolg^{-1} h^{-1} within 1 h, representing an 8.1-fold enhancement compared to TP-AN-COF (606 μmol g^{-1} h^{-1}) (Fig. 3c). After normalization by surface area, the H_2O_2 production rate of the TP-PZ-COF catalyst reaches 4.8 μmol m^{-2} h^{-1}, whereas that of the TP-AN-COF catalyst is only 0.63 μmol m^{-2} h^{-1}. Considering that H_2O_2 may undergo slight disproportionation under alkaline conditions, we performed control experiments to evaluate its stability at pH 12 (Fig. S11 and S12†). In the absence of catalysts, H_2O_2 remained relatively stable in the dark but showed a modest decrease under light irradiation. Upon introducing the COF catalysts, H_2O_2 decayed more rapidly; notably, TP-AN-COF induced a more pronounced decline, whereas TP-PZ-COF resulted in a comparatively slower decrease. These results indicated that H_2O_2 experiences minor decomposition under alkaline light-irradiated conditions; nevertheless, TP-PZ-COF still delivered higher net H_2O_2 accumulation during photocatalysis. Impressively, TP-PZ-COF demonstrated excellent recyclability, maintaining high activity over five consecutive photocatalytic cycles with only a slight decline in H_2O_2 production (Fig. 3d).

View Article Online
DOI: 10.1039/D5SC08293F

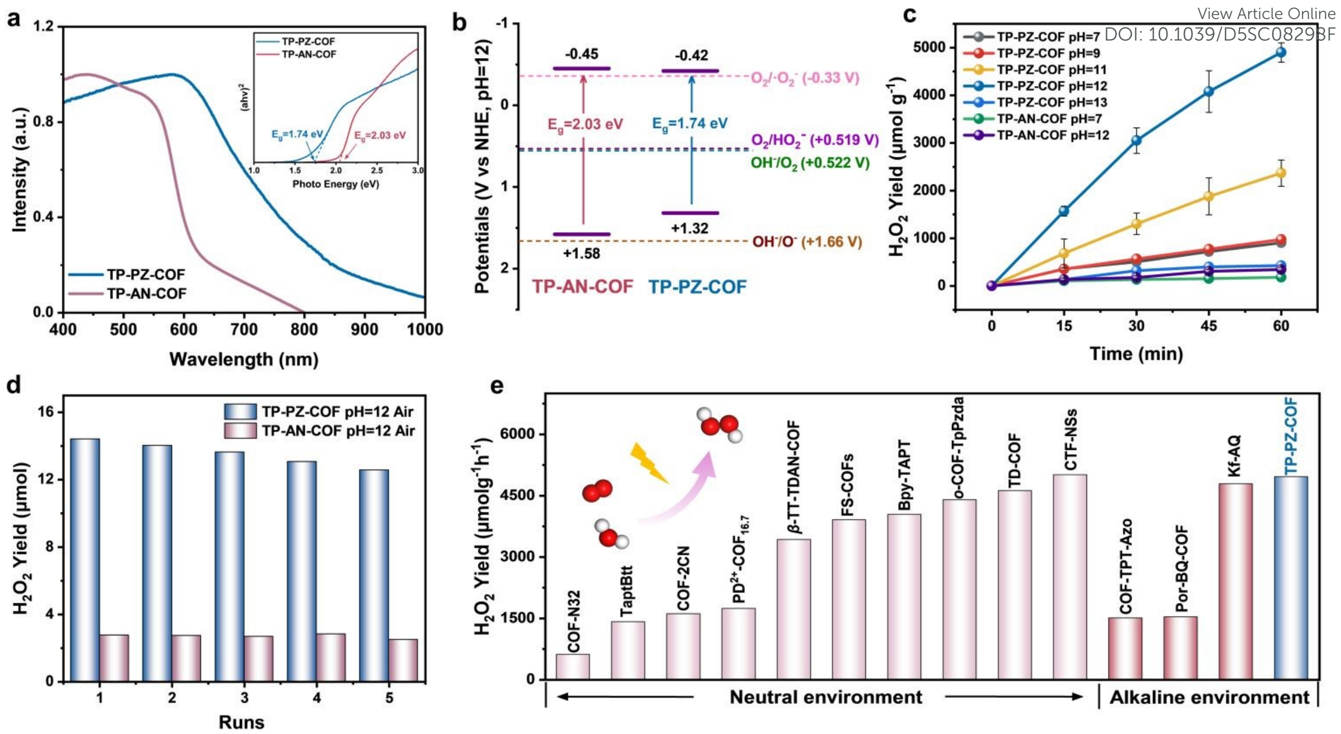

Fig. 3 (a) UV/vis diffusion absorption spectra and Tauc plot (inset); (b) Experimentally derived energy band alignments; (c) Photocatalytic H_2O_2 yield rates for TP-PZ-COF and TP-AN-COF. (d) Cycling performance of TP-PZ-COF and TP-AN-COF. (e) Summarized H_2O_2 production rate in different environments.

The FT-IR, ^{13}C NMR and PXRD spectra achieved no noticeable changes after multiple photocatalytic cycles, further confirming the structural stability of TP-PZ-COF and TP-AN-COF during continuous H_2O_2 production in 0.01 M NaOH (Fig. S13, S14, S15, S16, S17 and S18†). Moreover, its apparent quantum yield (AQY) reached 2.53% at 600 nm, consistent with its visible-light absorption profile (Fig. S19†). Under simulated solar illumination (AM 1.5G), TP-PZ-COF achieved a solar-to-chemical conversion (SCC) efficiency of 0.72%, outperforming most previously reported COF-based photocatalysts (Fig. 3e and Table S3). Moreover, TP-PZ-COF maintained stable H_2O_2 production under continuous light irradiation (Fig. S20†). Under natural sunlight irradiation (10:30 a.m. to 4:30 p.m.), the system achieved a cumulative H_2O_2 yield of 16.6 μmol over 6 h, representing a ~9.3-fold increase compared to TP-AN-COF (Fig. S21†). To enhance practical applicability, TP-PZ-COF was uniformly incorporated into a polyacrylamide (PAAm) hydrogel matrix, affording a COF–hydrogel film with a side length of 2 cm (Fig. S22†).[42] Under simulated sunlight, the resulting film achieved an outstanding H_2O_2 production rate of 55.4 mmolh^{-1} m^{-2}. Also, the solution collected after 6 hours of light irradiation of the film was applied to simulated industrial dye wastewater containing Rhodamine B (Rh B) and Rose Bengal (RB), exhibiting a remarkable purification performance (Fig. S23 and S24†).[43] This strategy may pave the way for the practical application of photocatalytic systems in alkaline aqueous environments. Additionally, we prepared two phenazine-based COFs with different *β*-ketoenamine densities, DP-PZ-COF and HP-PZ-COF, to probe the influence of *β*-ketoenamine tautomerization on photocatalytic H_2O_2 production under alkaline conditions (Fig. S25 and S26†). The H_2O_2 generation rates in alkaline media reveal that decreasing the *β*-ketoenamine density leads to a gradual decline in photocatalytic efficiency. Remarkably, DP-PZ-COF (610 μmolg^{-1} h^{-1}) and HP-PZ-COF (456 μmolg^{-1} h^{-1}) still outperform TP-AN-COF (340 μmolg^{-1} h^{-1}), further highlighting the crucial role of the phenazine unit in modulating molecular orbitals and stabilizing the hydrogen-bond network (Fig. S27†).

A series of control experiments were conducted under alkaline conditions to elucidate the reaction pathway of photocatalytic H_2O_2 generation.[44] As shown in Fig. S28†, negligible H_2O_2 was detected under either N_2 atmosphere or dark conditions, confirming that H_2O_2 formation in this system was primarily driven by light-induced 2e$^-$ ORR ($O_2 + 2e^- + H_2O \rightarrow HO_2^- + OH^-$), rather than 2e$^-$ WOR ($3OH^- \rightarrow HO_2^- + H_2O + 2e^-$). To identify the reactive species Involved in the redox process, quenching experiments were performed using potassium dichromate ($K_2Cr_2O_7$), benzyl alcohol (BA), and *p*-benzoquinone (*p*-BQ) as scavengers for electrons (e$^-$), holes (h$^+$), and superoxide radicals ($\cdot O_2^-$), respectively (Fig. 4a). In the presence of $K_2Cr_2O_7$, both COFs produced negligible amounts of H_2O_2, corroborating the electron-driven nature of the ORR pathway. Online gas analysis further confirmed that O_2 evolution via the 4e$^-$ WOR was remarkably promoted under alkaline of 18.57 μmol h^{-1}, nearly 4-fold higher than that of TP-AN-COF (4.70 μmol h^{-1}), which was ascribed to the superior OH^- adsorption capacity and lower energy barrier for the 4e$^-$ WOR pathway of the PZ unit (Fig. S29†). Upon the addition of BA, the H_2O_2 production rate of TP-AN-COF increased markedly from 606 to 1957 μmolg^{-1} h^{-1} (3.2-fold), whereas TP-PZ-COF showed only a slight enhancement (from 3003 to 3234 μmolg^{-1} h^{-1}), indirectly suggesting that TP-PZ-COF possesses inherently stronger OH^- affinity. When excess p-BQ was introduced, H_2O_2 generation by both COFs was largely suppressed due to the quenching of $\cdot O_2^-$, indicating that $\cdot O_2^-$ is a key intermediate in the

View Article Online
DOI: 10.1039/D5SC08298F

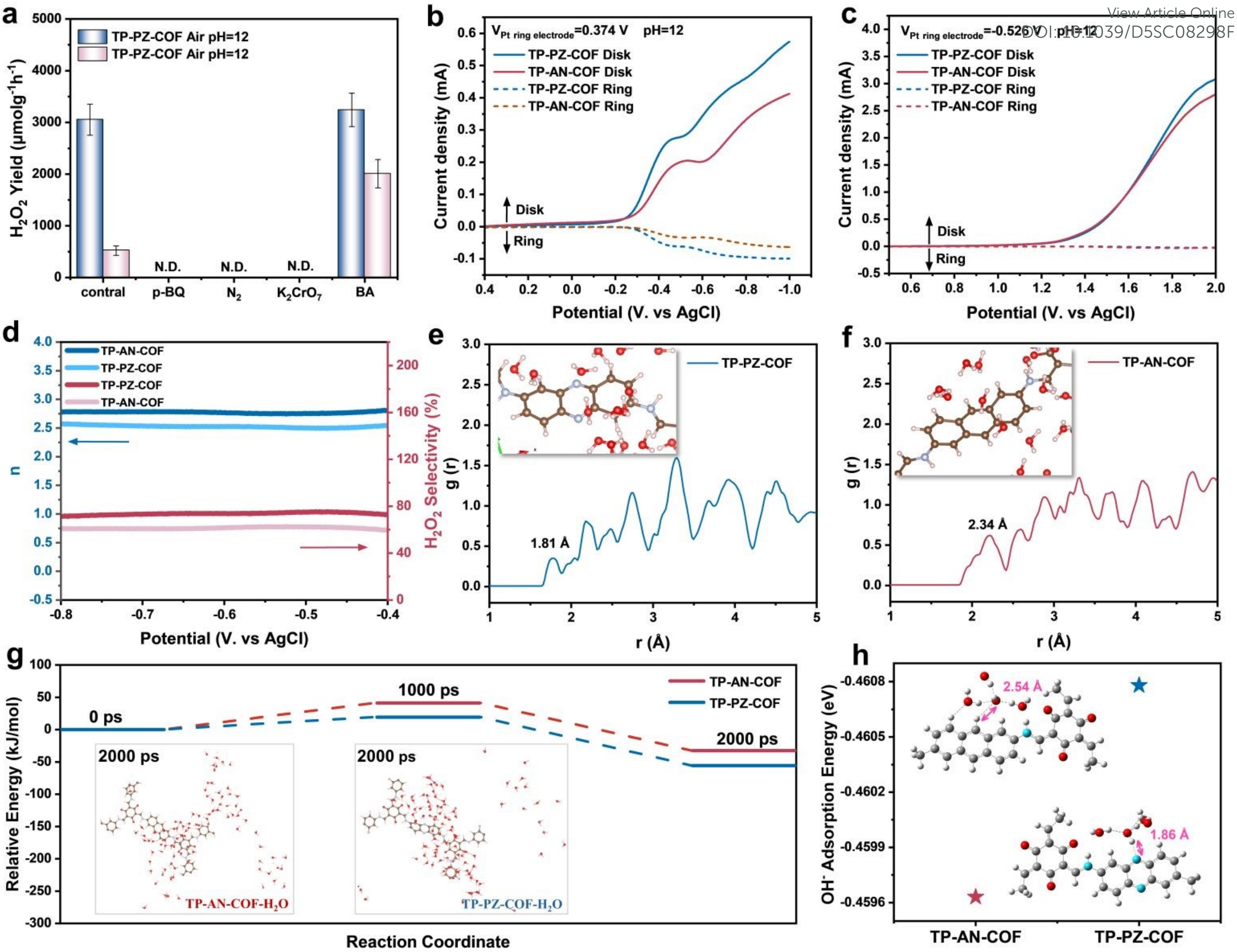

Fig. 4 (a) Comparison of H_2O_2 production rates by TP-PZ-COF and TP-AN-COF under different conditions. (b) The potential of the Pt ring electrode was set to 0.374 V vs. Ag/AgCl for the detection of H_2O_2. (c) The potential of the Pt ring electrode was set to –0.526 V vs. Ag/AgCl for the detection of O_2. (d) the ORR electron transfer number calculated from RRDE measurement of in O_2 pre-saturated 0.01 M NaOH and H_2O_2 selectivity of TP-AN-COF and TP-PZ-COF. Radial distribution functions (AIMD) of water with respect to. (e) C center of TP-AN-COF and f) N center of TP-PZ-COF. (g) Time-resolved relative energy profiles of TP-PZ-COF and TP-AN-COF. (h) The adsorption energy of $(H_2O)_3OH^-$ for TP-PZ-COF and TP-AN-COF.

ORR pathway. Electron paramagnetic resonance (EPR) spectroscopy with 5,5-Dimethyl-1-pyrroline N-oxide (DMPO) as a spin-trapping agent offered independent verification of the generation of $\cdot O_2^-$ under light irradiation (Fig. S30†), supporting a stepwise 1e⁻ reduction mechanism for H_2O_2 formation in both systems. Overall, TP-PZ-COF demonstrated considerably enhanced photocatalytic H_2O_2 production efficiency under alkaline conditions compared to TP-AN-COF. Rotating ring-disk electrode (RRDE) analysis revealed that TP-PZ-COF delivered a lower water-generation current and a superior 2e⁻ ORR H_2O_2 generation current than TP-AN-COF (Fig. 4b). Moreover, pH-corrected electrochemical analysis of WOR revealed a significantly higher O_2 evolution current for TP-PZ-COF compared to TP-AN-COF (Fig. 4c), consistent with its enhanced 4e⁻ WOR activity. According to the Levich equation, the average electron transfer numbers (n) during ORR were calculated to be 2.5 for TP-PZ-COF and 2.8 for TP-AN-COF (Fig. 4d), implying that TP-PZ-COF preferentially undergoes the 2e⁻ ORR pathway. As shown in Fig. 4h, TP-PZ-COF achieved a high H_2O_2 selectivity of ~75% within the potential range of −0.4 to −0.8 V, significantly higher than that of TP-AN-COF (~62%). This distinct difference highlights the kinetic preference of TP-PZ-COF for selective 2e⁻ ORR ($O_2 + 2e^- + H_2O \rightarrow HO_2^- + OH^-$) and 4e⁻ WOR ($4OH^- \rightarrow O_2 + 2H_2O + 4e^-$) processes, thus enabling more efficient and selective H_2O_2 production.

To gain deeper insights into the interactions between $(H_2O)_nOH^-$ clusters, molecular O_2, and the PZ moieties, AIMD simulations were performed by placing COF fragments in an explicit alkaline aqueousenvironment.[45, 46] As shown in Fig. 4e and 4f, radial distribution function (RDF) analysis revealed a significantly shorter hydrogen- bonding distance between H_2O molecules and the PZ units in TP-PZ-COF (1.81 Å) compared to the AN-based TP-AN-COF (2.34 Å), suggesting stronger hydrogen-bonding interactions. These enhanced interactions likely promoted OH^- transport via the Grotthuss mechanism, thereby facilitating more efficient photocatalytic H_2O_2 production.[47] Contact angle measurements also

View Article Online
DOI: 10.1039/D5SC08298F

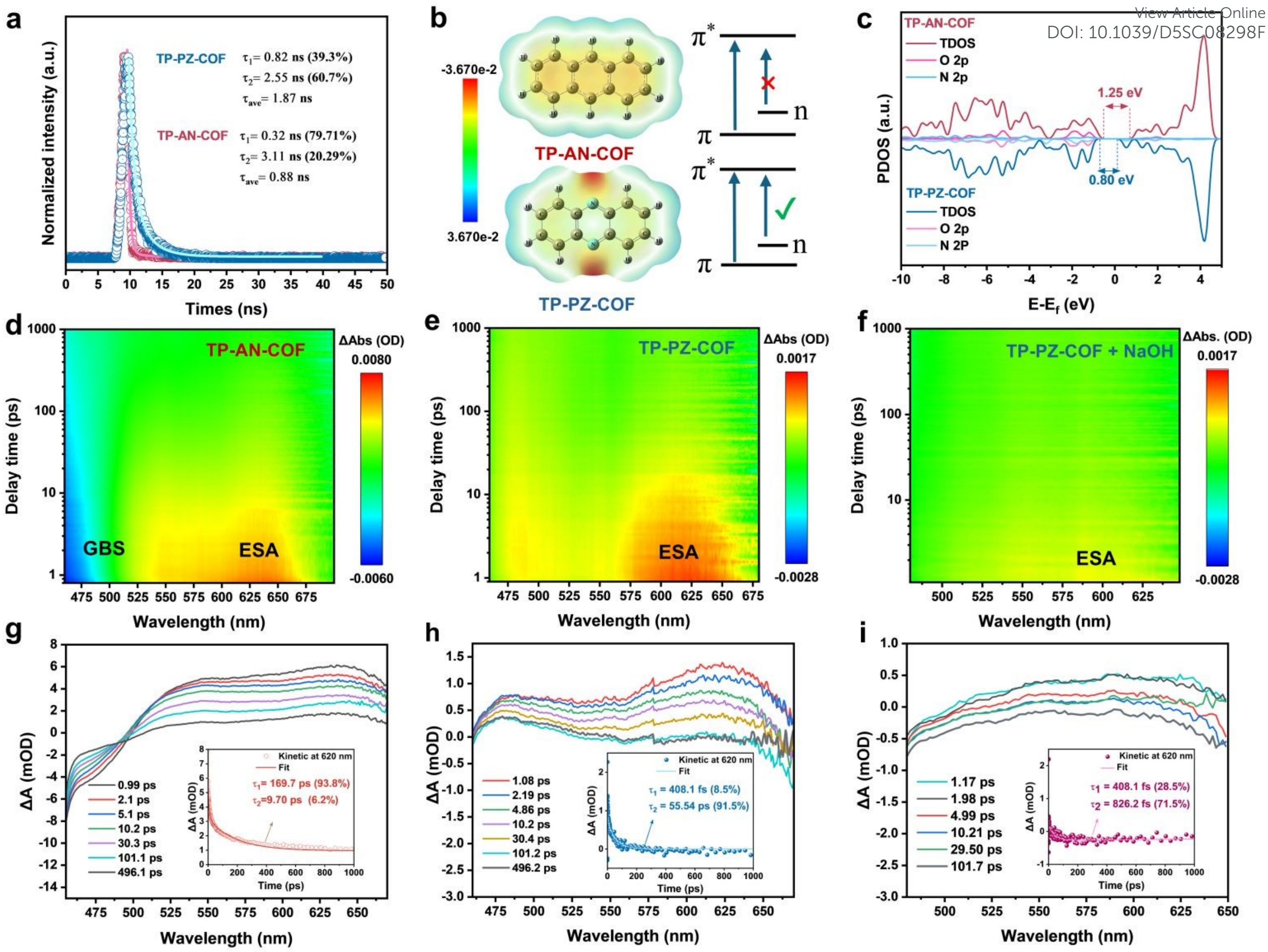

Fig. 5 (a) Time-resolved PL decay spectra of TP-PZ-COF and TP-AN-COF, excited at 375 nm. (b) Electrostatic surface potential maps and molecular orbital transitions of PZ unit and anthracene unit. (c) PDOS analysis for TP-PZ-COF and TP-AN-COF. fs-TA two-dimensional pseudocolor maps of (d) TP-AN-COF, (e) TP-PZ-COF, (f) TP-PZ-COF dispersed in 0.01 M NaOH aqueous solution. Kinetic traces at 620 nm extracted from the femtosecond transient absorption spectra of (g) TP-AN-COF, h) TP-PZ-COF, and (i) TP-PZ-COF in 0.01 M NaOH.

confirmed the conclusion that the improved surface hydrophilicity of TP-PZ-COF (Fig. S31†). Moreover, the relative energies of the two COFs were tracked over a 5.5 ns AIMD simulation (Fig. 4g, S32 and S33†). At 2000 ps, TP-PZ-COF exhibited a lower energy state and a higher number of surrounding water molecules, suggesting stronger interactions with the adjacent $(H_2O)_nOH^-$ clusters. Consistent with these findings, DFT calculations demonstrated that TP-PZ-COF showed a superior binding affinity toward the $(H_2O)_3OH^-$ cluster at its PZ sites (Fig. 4i). These results align well with the superior $4e^-$ WOR performance of TP-PZ-COF and underscore the critical role of PZ moieties in enhancing OH^- adsorption and transport under alkaline conditions.[48]

The origin of the distinct photocatalytic activities of the two COFs was further elucidated by systematically probing their charge-carrier dynamics under alkaline conditions. Electrochemical impedance spectroscopy (EIS) and transient photocurrent (i–t) measurements show that TP-PZ-COF delivers a markedly higher photocurrent response and a lower charge-transfer resistance than TP-AN-COF, consistent with more efficient charge transport and interfacial charge transfer (Fig. S34 and S35†). In addition, photoluminescence (PL) spectroscopy revealed a substantially weaker emission for TP-PZ-COF (Fig. S36†), suggesting suppressed radiative recombination and enhanced charge separation. These observations are further supported by fluorescence lifetime (FLT) measurements, where TP-PZ-COF exhibited a longer excited-state lifetime than TP-AN-COF, indicative of a higher fraction of long-lived charge carriers (Fig. 5a). DFT calculations provided additional insights into the electronic structures. In addition to the typical $\pi \rightarrow \pi^*$ transitions of aromatic rings, the sp^2-hybridized nitrogen atoms in the PZ units of TP-PZ-COF possess non-bonding lone-pair electrons, enabling $n \rightarrow \pi^*$ transitions with adjacent aromatic carbons.[49] This orbital coupling lowers the excitation energy and is expected to promote preferential localization of photoexcited electrons on the PZ moieties (Fig. 5b). The longer τ_2 indicates a slower carrier recombination process, while the partial density of states (PDOS) analysis revealed an increased density of p-orbital electrons near the valence band edge in TP-PZ-COF, effectively narrowing the bandgap and facilitating exciton dissociation (Fig. 5c).

View Article Online
DOI: 10.1039/D5SC08298F

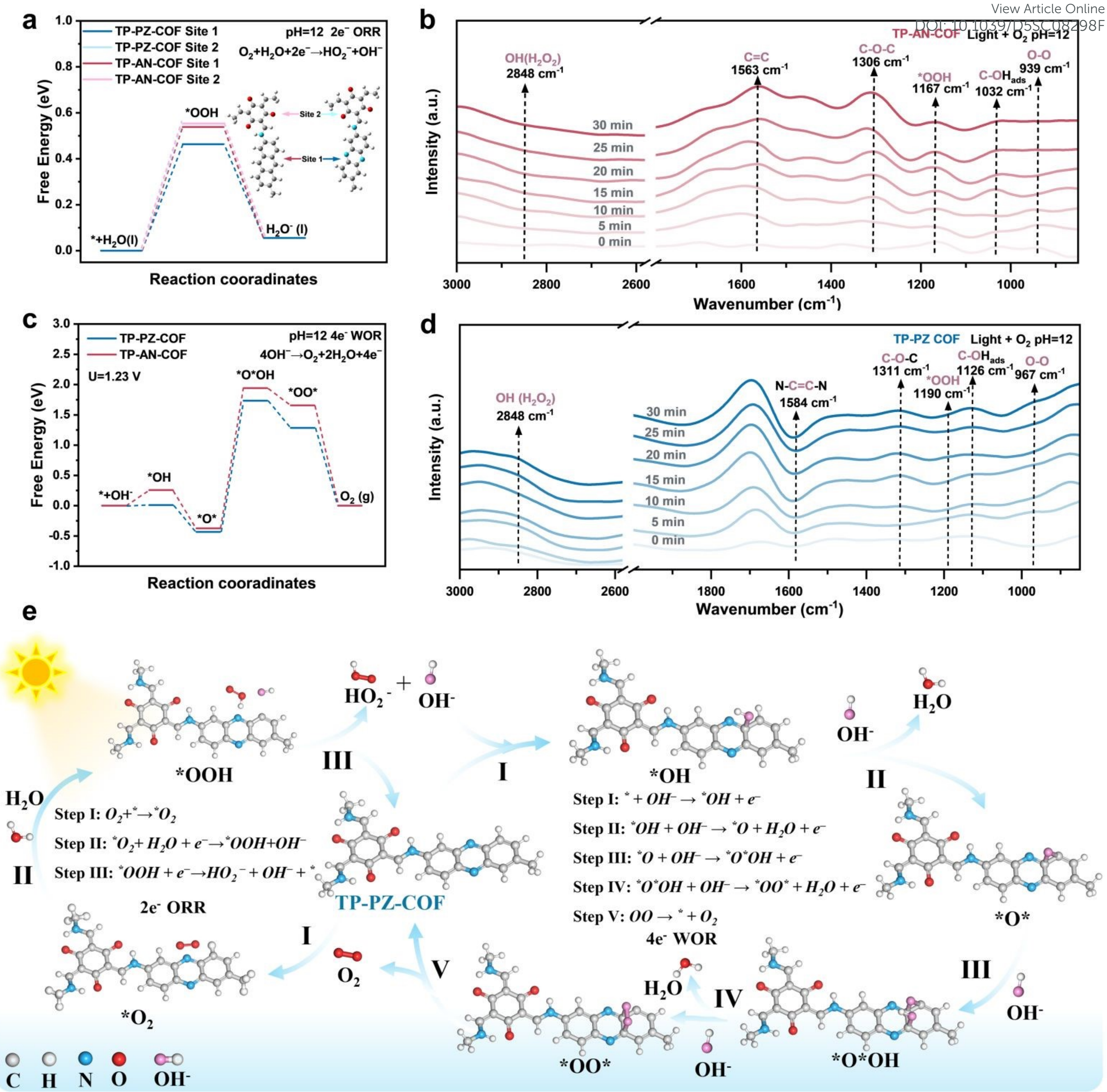

Fig. 6 (a) Free-energy diagrams for a stepwise 1e⁻ ORR to H_2O_2 on the TP-AN-COF and TP-PZ-COF. (b) in situ DRIFT spectra recorded during photocatalytic H_2O_2 production on TP-AN-COF. (c) Calculated free energy diagrams of WOR pathway in both COFs. (d) in situ DRIFT spectra recorded during photocatalytic H_2O_2 production on TP-AN-COF. (e) Schematic illustration of the overall H_2O_2 production mechanism over TP-PZ-COF

To investigate the impact of the n→π* transition on excited-state carrier dynamics in TP-PZ-COF and TP-AN-COF, fs-TAS was employed. Upon excitation with a 420 nm pump pulse, two-dimensional pseudocolor maps (Fig. 5d and 5e) and representative decay profiles over a delay range of 1–500 ps (Fig. 5g and 5h) were obtained. For TP-AN-COF, a distinct ground-state bleaching (GSB) signal was observed at 475 nm, along with an excited-state absorption (ESA) band at 620nm. In contrast, TP-PZ-COF exhibited positive ESA signals at both 475 and 620 nm. Kinetic fitting of the time-resolved signals at 620 nm using a biexponential model yielded two decay components for each sample. For TP-AN-COF, the lifetimes were τ_1 = 169.7 ps (93.8%) and τ_2 = 9.70 ps (6.2%) (Fig. 5g, inset), while TP-PZ-COF showed τ_1 = 408.1 fs (8.5%) and τ_2 = 55.54 ps (91.5%) (Fig. 5h, inset). The shorter τ_1 for TP-PZ-COF may be associated with faster relaxation of hot electrons toward the CB minimum, thereby potentially facilitating the availability of photogenerated electrons for subsequent redox processes. In comparison, TP-PZ-COF shows a noticeably longer τ_2 than TP-AN-COF, suggesting an increased population of longer-lived charge carriers that could reach the surface and contribute to ORR and WOR. Moreover, upon addition of 10% NaOH solution (pH = 12), the ESA signal of TP-PZ-COF was significantly attenuated (Fig.5i), accompanied by a sharp decrease in τ_2 to 826.2 fs (71.5%), indicating efficient quenching of photoexcited electrons by OH^- species. Interestingly, visible O_2 bubble formation was observed under 420 nm laser irradiation, confirming the photocatalytic activity (Fig. S37†). Collectively, these findings highlight the superior charge separation efficiency and extended lifetime of active electrons in TP-PZ-COF, contributing to enhanced photocatalytic performance.

Guided by DFT calculations and spectroscopic analyses, the critical role of PZ units in modulating electron distribution and charge transfer in TP-PZ-COF was established, prompting investigations to elucidate its catalytic mechanism for H_2O_2 production under alkaline conditions. Experimental results demonstrated that both COFs followed a stepwise $1e^-$ ORR pathway involving molecular oxygen and intermediates such as $^*OOH$ ($O_2 + H_2O + 1e^- \rightarrow {}^*OOH + OH^-$; $^*OOH + 1e^- \rightarrow HO_2^-$). To probe the intrinsic differences in ORR active sites between the two materials, detailed Gibbs free energy (ΔG) analyses were performed. In TP-AN-COF, TFP moiety revealed the more favorable ΔG for $^*OOH$ formation compared to the AN unit, suggesting it as the predominant ORR active site (Fig. 6a).[50] In contrast, the PZ moiety in TP-PZ-COF was identified as the most favorable site, highlighting its superior capability for H_2O and O_2 adsorption and activation under alkaline conditions. These results were further corroborated by FTIR spectroscopy. Upon immersion in water, the characteristic phenazine-associated peak in TP-PZ-COF exhibited a redshift from 1163.5 cm^{-1} to 1069.4 cm^{-1}, whereas the peaks corresponding to AN units remained unchanged (Fig. S38 and S39†). This spectral shift indicates strong N···H–O hydrogen bonding interactions at the PZ site, facilitating $^*H$ dissociation and subsequent O_2 activation to form $^*OOH$ intermediates. Furthermore, DRIFTS measurements provided direct evidence for the stepwise $1e^-$ ORR mechanism. As shown in Fig. 6b and 6d, characteristic $^*OOH$ signals appeared at ~1167 and ~1190 cm^{-1}, while O–O vibrational modes were observed at ~939 and ~967 cm^{-1} in TP-AN-COF and TP-PZ-COF, respectively.[51] Also, a newly emerging peak at ~2838 cm^{-1}, attributed to the O–H stretching vibration of H_2O_2, increased in intensity under visible light irradiation over time, serving as direct spectroscopic evidence for photocatalytic H_2O_2 production.[52]

Under alkaline conditions, the $4e^-$ WOR leading to O_2 evolution becomes thermodynamically more favorable compared to neutral environments.[53]In contrast to neutral conditions that generally necessitate water deprotonation, the alkaline WOR pathway proceeds via direct OH^- adsorption, yielding $^*OH$ intermediates, which subsequently evolve through $^*O^*$, $^*O^*OH$, and $^*OO^*$ species in a stepwise manner.[54] DFT calculations revealed that, in TP-PZ-COF, the C atoms adjacent to N atoms within the PZ units possess more positive electrostatic potential due to the high electronegativity of N (Fig. S40†). As a result, the $^*OH$ formation on the PZ sites of TP-PZ-COF is more favorable than on the conventional AN moiety, with a reduced ΔG by approximately 0.25 eV. This finding suggests that the incorporation of PZ units effectively modulates the WOR energy landscape, thereby enhancing the overall H_2O_2 production efficiency. Additional evidence was provided by in situ DRIFTS measurements. As shown in Fig. 6b and 6d, the absorption bands at ~1032 and ~1126 cm^{-1} are attributed to surface-bound C–OH_{ads} intermediates, confirming the initial OH^- adsorption step in the WOR process. In addition, a distinct vibration at ~1300 cm^{-1} corresponds to the formation of C–O–C species, indicating the generation of $^*O^*$ intermediates in both COFs.[55] Notably, the pronounced attenuation of the C=C stretching vibration at ~1584 cm^{-1}, attributed to the PZ moiety, upon photoirradiation further substantiates the involvement of aromatic C=C as active sites in the $4e^-$ WOR pathway for O_2 evolution ($4OH^- \rightarrow O_2 + 2H_2O + 4e^-$).

Combined insights from in situ spectroscopic analyses and DFT calculations provide an improved understanding of the H_2O_2 formation pathways in both COFs. As illustrated in Fig. S41† and Fig. 6e, a mechanistic model is proposed for the photocatalytic production of H_2O_2 over TP-AN-COF and TP-PZ-COF under alkaline conditions. In TP-AN-COF, the hydrophilic TFP unit is identified as the active site for a stepwise $1e^-$ ORR pathway, where surface C=O moieties initially form weak hydrogen bonds with H_2O, facilitating $^*H$ capture by O_2 to generate the $^*OOH$ intermediate, which then dissociates into HO_2^- and OH^- ($O_2 + H_2O + 1e^- \rightarrow {}^*OOH + OH^-$; $^*OOH + 1e^- \rightarrow HO_2^-$). The liberated OH^- species can be adsorbed by the aromatic rings on the AN unit, promoting a $4e^-$ WOR to evolve O_2 ($4OH^- \rightarrow O_2 + 2H_2O + 4e^-$). Notably, the evolved O_2 may be reused in the ORR, forming a catalytic cycle. In contrast, the PZ unit in TP-PZ-COF is proposed to act as a bifunctional active site that simultaneously promotes the $2e^-$ ORR and the $4e^-$ WOR.The nitrogen atoms in the PZ ring can stabilize O_2 and $(H_2O)_nOH^-$ via strong hydrogen bonding, which promotes the formation of $^*OOH$ intermediates and their subsequent dissociation into HO_2^- and OH^-. The resulting OH^- is favorably adsorbed by adjacent carbon atoms, forming $^*OH$ intermediates that proceed through $^*O^*OH$ and $^*OO^*$ species to produce O_2. This O_2 can subsequently re-enter the ORR cycle. Such cooperative ORR/WOR catalytic behavior centered on the PZ moiety is key to the superior H_2O_2 production efficiency observed for TP-PZ-COF under alkaline conditions. These findings underscore the pivotal role of the PZ unit in H_2O_2-oriented COF design, offering a dual advantage of enhanced charge carrier kinetics and robust hydrogen-bonding frameworks.

Conclusion

By employing a dual-regulation strategy of molecular orbital engineering and hydrogen-bonding network design, we successfully designed and synthesized a phenazine-based covalent organic framework (TP-PZ-COF) capable of efficient overall photocatalytic H_2O_2 production from alkaline aqueous solution and O_2 via a synergistic $2e^-$ ORR and $4e^-$ WOR. Experimental results revealed that the PZ moiety plays a crucial role in enhancing photogenerated charge utilization and constructing a stable hydrogen-bonding network, thereby facilitating efficient exciton separation and directional OH^- transport, which collectively boost photocatalytic H_2O_2 production. Further DFT and AIMD calculations confirmed that the incorporation of the PZ unit significantly lowers the energy barriers for both the stepwise $1e^-$ ORR pathway to form H_2O_2 and the $4e^-$ WOR pathway to evolve O_2, providing a theoretical basis for the excellent photocatalytic activity of TP-PZ-COF. Moreover, the integration of TP-PZ-COF with polyacrylamide further expands its application potential in the purification of industrial dye wastewater. This work not only offers a new perspective for sustainable H_2O_2 production in basic media but also provides valuable insights into the

View Article Online
DOI: 10.1039/D5SC08298F

rational design of metal-free COF-based photocatalysts for O_2-to-H_2O_2 conversion.

Author Contributions

Z. Yu conceived and designed the research. J. Zhang and X. Zhang assisted in catalyst synthesis and conducted the photocatalytic activity tests. X. Sun and Z. Yu carried out the material characterization and fs-TAS measurements. G.W. performed the DFT calculations. Z. Yu wrote the manuscript under the supervision of F. Yu and J. Hua. All authors discussed the results and contributed to the manuscript revision.

Conflicts of interest

The authors declare no conflict of interest.

Data availability

The data that support the findings of this study are available from the corresponding author upon reasonable request.

Acknowledgements

For financial support of this research, the authors thank the projects supported by the National Natural Science Foundation of China (22271093, 21971064, 22105034, 22465001), Young Elite Scientists Sponsorship Program by JXAST (2024QT11), the Science and Technology Commission of Shanghai Municipality (24DX1400200), the Programme of Introducing Talents of Discipline to Universities (B16017) and the Fundamental Research Funds for the Central Universities. The authors thank the Research Center of Analysis and Test of East China University of Science and Technology for the help on the characterization.

Notes and references

1. F. Y. Yu, Y. J. Zhou, H. Q. Tan, Y. G. Li and Z. H. Kang, *Adv. Energy Mater.*, 2023, **13**, 2300119.
2. Y. Chen, Y. Guo, T. Wang, S. Ji, H. Shao, M. Lin, S. Seki, N. Yan and D. Jiang, *Nat. Commun.*, 2025, **16**, 6495.
3. B. Mishra, A. Alam, A. Chakraborty, B. Kumbhakar, S. Ghosh, P. Pachfule and A. Thomas, *Adv. Mater.*, 2024, 2413118.
4. Z. Chen, H. Weng, C. Chu, D. Yao, Q. Li, C. Zhang and S. Mao, *Nat. Commun.*, 2025, **16**, 6943
5. H. Yan, Y. Peng, Y. Huang, M. Shen, X. Wei, W. Zou, Q. Tong, N. Zhou, J. Xu, Y. Zhang, Y. X. Ye and G. Ouyang, *Adv. Mater.*, 2024, **36**, 2311535.
6. A. Alam, B. Kumbhakar, A. Chakraborty, B. Mishra, S. Ghosh, A. Thomas and P. Pachfule, *ACS Mate. Lett.*, 2024, **6**, 2007-2049.
7. J. Fu, S. Xiao, J. Cao, Z. Liang, J. Chen, Y. Jiang and M. Xing, *Angew. Chem., Int. Ed.*, 2025, **64**, e202421800.
8. Y. Chen, R. Liu, Y. Guo, S. W. Yang and D. Jiang, *Nat. Synth.*, 2024, **3**, 998-1010.
9. Z. Yu and J. Hua, *ACS Appl. Energy Mater.*, 2025, **8**, 8830-8849.
10. H. H. Sun, Z. B. Zhou, Y. Fu, Q. Y. Qi, Z. X. Wang, S. Xu and X. Zhao, *Angew. Chem., Int. Ed.*, 2024, **63**, e202409250.
11. A. P. Coˆte´, A. I. Benin, N. W. Ockwig, M. O'Keeffe, A. J. Matzger and O. M. Yaghi, *Science*, 2005, **310**, 1166.
12. Y. Chen and D. Jiang, *Acc. Chem. Res.*, 2024, **57**, 3182-3193.
13. R. R. Liang, S. Y. Jiang, R. H. A and X. Zhao, *Chem. Soc. Rev.*, 2020, **49**, 3920-3951.
14. Q. Guan, L.-L. Zhou and Y.-B. Dong, *J. Am. Chem. Soc.*, 2023, **145**, 1475-1496.
15. H. Zhuang, C. Guo, J. Huang, L. Wang, Z. Zheng, H. N. Wang, Y. Chen and Y. Q. Lan, *Angew. Chem., Int. Ed.*, 2024, **63**, e202404941.
16. Y. Liu, X. Liu, A. Su, C. Gong, S. Chen, L. Xia, C. Zhang, X. Tao, Y. Li, Y. Li, T. Sun, M. Bu, W. Shao, J. Zhao, X. Li, Y. Peng, P. Guo, Y. Han and Y. Zhu, *Chem. Soc. Rev.*, 2024, **53**, 502-544.
17. H. He, R. Shen, Y. Yan, D. Chen, Z. Liu, L. Hao, X. Zhang, P. Zhang and X. Li, *Chem, Sci.*, 2024, **15**, 20002-20012.
18. X. Sun, J. Yang, X. Zeng, L. Guo, C. Bie, Z. Wang, K. Sun, A. K. Sahu, M. Tebyetekerwa, T. E. Rufford and X. Zhang, *Angew. Chem., Int. Ed.*, 2024, **63**, e202414417.
19. X. Yu, Z. Wei, Y. Qin, X. Zhang, D. Hao, L. Jing, Y. Liu, H. Dai, J. Deng and Y. Zhu, *Adv. Mater.*, 2025, **37**, 2501494.
20. H. Ma, Y. Zhang, Y. Wu, Q. Gu, Z. Li and Q. Zhang, *Chem. Sci.*, 2025, **16**, 16668-16677.
21. J.-Y. Yue, Z.-X. Pan, Y. Guo, P. Yang and B. Tang, *Chem. Sci.*, 2025, **16**, 13883-13892.
22. Y. Liu, L. Li, Z. Sang, H. Tan, N. Ye, C. Sun, Z. Sun, M. Luo and S. Guo, *Nat. Synth.*, 2024, **4**, 134-141.
23. T. Xu, Z. Wang, W. Zhang, S. An, L. Wei, S. Guo, Y. Huang, S. Jiang, M. Zhu, Y.-B. Zhang and W.-H. Zhu, *J. Am. Chem. Soc.*, 2024, **146**, 20107-20115.
24. X. Ma, H. Pan, L. Gong, X. Ding, X. Zhou, H. Liu, R. Wang, C. Qu, Y. Zhao, D. Qi, Y. Bian and J. Jiang, *Angew. Chem., Int. Ed.*, 2025, **64**, e202511024.
25. H. Liu, S. Zhu, Y. Zhi, H. Yue and X. Liu, *Chem. Sci.*, 2025, **16**, 12768-12803.
26. W. Zhang, M. Sun, J. Cheng, X. Wu and H. Xu, *Adv. Mater.*, 2025, **37**, 2500913.
27. R. Liu, D. Zhao, S. Ji, H. Shao, Y. Chen, M. Feng, T. Wang, J. Li, M. Lin, T. C. Sum, N. Yan, S. Seki and D. Jiang, *Nat. Mater.*, 2025, **24**, 1245-1257.
28. X. Lu, Y. Zhang, X. Ma, C. Yuan, Y. Chen, J. Guo, D. Gao, Y. Tu, Q. Liu, J. Wang and Z. Wei, *Angew. Chem., Int. Ed.*, 2025, **64**, e202503372.
29. Q. Liu, T. Tang, Z. Tian, S. Ding, L. Wang, D. Chen, Z. Wang, W. Zheng, H. Lee, X. Lu, X. Miao, L. Liu and L. Sun, *Nat. Commun.*, 2024, **15**, 6722.
30. Q. Wang, Y. Gong, X. Zi, L. Gan, E. Pensa, Y. Liu, Y. Xiao, H. Li, K. Liu, J. Fu, J. Liu, A. Stefancu, C. Cai, S. Chen, S. Zhang, Y. R. Lu, T. S. Chan, C. Ma, X. Cao, E. Cortés and M. Liu, *Angew. Chem., Int. Ed.*, 2024, **63**, e202405438.
31. E. Vitaku, C. N. Gannett, K. L. Carpenter, L. Shen, H. D. Abruña and W. R. Dichtel, *J. Am. Chem. Soc.*, 2019, **142**, 16-20.
32. S. Feng, L. Wang, L. Tian, Y. Liu, K. Hu, H. Xu, H. Wang and J. Hua, *Chem. Sci.*, 2024, **15**, 11972-11980.
33. Z. Hirani, N. M. Schweitzer, E. Vitaku and W. R. Dichtel, *Angew. Chem., Int. Ed.*, 2025, **64**, e202502799.
34. R. Liu, Y. Chen, H. Yu, M. Položij, Y. Guo, T. C. Sum, T. Heine and D. Jiang, *Nat. Catal.*, 2024, **7**, 195-206.
35. T. Yang, D. Zhang, A. Kong, Y. Zou, L. Yuan, C. Liu, S. Luo, G. Wei and C. Yu, *Angew. Chem., Int. Ed.*, 2024, **63**, e202404077.
36. H. Hou, K. Wu, X. Chen, X. Liu and Y. Zhao, *J. Am. Chem. Soc.*, 2025, **147**, 27835-27846
37. Y. Wan, L. Wang, H. Xu, X. Wu and J. Yang, *J. Am. Chem. Soc.*, 2020, **142**, 4508-4516.
38. G. Jerkiewicz, *ACS Catal.*, 2020, **10**, 8409-8417.
39. N. H. Kwon, M. Kim, X. Jin, J. Lim, I. Y. Kim, N.-S. Lee, H. Kim and S.-J. Hwang, *NPG Asia Mater.*, 2018, **10**, 659-669.
40. X. Ge, A. Sumboja, D. Wuu, T. An, B. Li, F. W. T. Goh, T. S. A. Hor, Y. Zong and Z. Liu, *ACS Catal.*, 2015, **5**, 4643-4667.
41. Z. Yong and T. Ma, *Angew. Chem., Int. Ed.*, 2023, **62**, e202308980.

42. Y. S. Zhang and A. Khademhosseini, *Science*, 2017, **356**, eaaf3627.
43. Z. Zhang, Q. Zhang, Y. Hou, J. Li, S. Zhu, H. Xia, H. Yue and X. Liu, *Angew. Chem., Int. Ed.*, 2024, **63**, e202411546.
44. Z. Yu, F. Yu, M. Xu, S. Feng, J. Qiu and J. Hua, *Adv. Sci.*, 2025, **12**, 2415194.
45. P. Li, Y. Jiang, Y. Hu, Y. Men, Y. Liu, W. Cai and S. Chen, *Nat. Catal.*, 2022, **5**, 900-911.
46. A. Chakraborty, A. Alam, U. Pal, A. Sinha, S. Das, T. Saha-Dasgupta and P. Pachfule, *Nat. Commun.*, 2025, **16**, 503.
47. W. Zheng, L. He, T. Tang, R. Ren, H. Lee, G. Ding, L. Wang and L. Sun, *Angew. Chem., Int. Ed.*, 2024, **63**, e202405738.
48. W. Li, Y. Ding, Y. Zhao, Z. Li, G. Lin, L. Wang and L. Sun, *Angew. Chem., Int. Ed.*, 2025, **64**, e202505924.
49. Y. Chen, Y. Cheng, Y. Liu, Y. Wang, Y. Qu, D. Jiang, Z. Qin and Y. Yuan, *Appl. Catal. B: Environ.*, 2024, **342**, 123453.
50. X. Zhang, S. Cheng, C. Chen, X. Wen, J. Miao, B. Zhou, M. Long and L. Zhang, *Nat. Commun.*, 2024, **15**, 2649.
51. Y. Hou, P. Zhou, F. Liu, Y. Lu, H. Tan, Z. Li, M. Tong and J. Ni, *Angew. Chem., Int. Ed.*, 2024, **63**, e202318562.
52. Q. Liao, Q. Sun, H. Xu, Y. Wang, Y. Xu, Z. Li, J. Hu, D. Wang, H. Li and K. Xi, *Angew. Chem., Int. Ed.*, 2023, **62**, e202310556.
53. J. Ding, D. Guo, N. Wang, H. F. Wang, X. Yang, K. Shen, L. Chen and Y. Li, *Angew. Chem., Int. Ed.*, 2023, **62**, e202311909.
54. R. Ram, L. Xia, H. Benzidi, A. Guha, V. Golovanova, A. G. Manjón, D. L. Rauret, P. S. Berman, M. Dimitropoulos, B. Mundet, E. Pastor, V. Celorrio, C. A. Mesa, A. M. Das, A. Pinilla-Sánchez, S. Giménez, J. Arbiol, N. López and F. P. G. d. Arquer, *Science*, 2024, **384**, 1373-1380.
55. J. Cheng, Y. Wu, W. Zhang, L. Wang, X. Wu and H. Xu, *Adv. Mater.*, 2024, **37**, 2410247.

View Article Online
DOI: 10.1039/D5SC08298F

View Article Online
DOI: 10.1039/D5SC08298F

Data availability

The data that support the findings of this study are available from the corresponding author upon reasonable request.